Field-induced water electrolysis switches an oxide semiconductor from an insulator to a metal

Hiromichi Ohta[1,2], Yukio Sato[3], Takeharu Kato[3], SungWng Kim[4], Kenji Nomura[4], Yuichi Ikuhara[3,5] & Hideo Hosono[4]

Water is composed of two strong electrochemically active agents, H^+ and OH^- ions, but has not been used as an active electronic material in oxide semiconductors. In this study, we demonstrate that water-infiltrated nanoporous glass electrically switches an oxide semiconductor from insulator to metal. We fabricated a field-effect transistor structure on an oxide semiconductor, $SrTiO_3$, using water-infiltrated nanoporous glass—amorphous $12CaO \cdot 7Al_2O_3$—as the gate insulator. Positive gate voltage, electron accumulation, water electrolysis and electrochemical reduction occur successively on the $SrTiO_3$ surface at room temperature. This leads to the formation of a thin (~3 nm) metal layer with an extremely high electron concentration (10^{15}–10^{16} cm^{-2}), which exhibits exotic thermoelectric behaviour. The electron activity of water as it infiltrates nanoporous glass may find many useful applications in electronics or in energy storage.

[1] Department of Applied Chemistry, Graduate School of Engineering, Nagoya University, Furo-cho, Chikusa, Nagoya 464–8603, Japan. [2] PRESTO, Japan Science and Technology Agency, 5 Sanbancho, Chiyoda, Tokyo 102–0075, Japan. [3] Nanostructures Research Laboratory, Japan Fine Ceramics Center, 2-4-1 Mutsuno, Atsuta, Nagoya 456–8587, Japan. [4] Frontier Research Center, Tokyo Institute of Technology, 4259 Nagatsuta, Midori, Yokohama 226–8503, Japan. [5] Institute of Engineering Innovation, The University of Tokyo, 2–11–16 Yayoi, Bunkyo, Tokyo 113–8656, Japan. Correspondence and requests for materials should be addressed to H.O. (email: h-ohta@apchem.nagoya-u.ac.jp).

Water has not been utilized as an active electronic material though water has been widely applied in industry as a coolant (radiators), solvent (batteries) and pressure medium (hydroelectric power generation). We have previously aimed to exploit the electrolysis of water[1]. Although the electrical conductivity of pure water is extremely low ($\sim$0.055 μS cm^{-1} at 25 °C)[2], ionization of H$^+$ and OH$^-$ ions occurs when the bias voltage ($>$1.23 V) is applied between two metallic electrodes immersed in water, as shown in Figure 1a. The ions are then attracted to the cathode and anode. Finally, H$_2$ and O$_2$ gases are generated on the cathode and anode, respectively, via the electron transfer on the electrode surface. As H$^+$ and OH$^-$ ions, which are strong reducing/oxidizing agents for most oxide semiconductors[3–8], are simultaneously produced in water electrolysis, one may expect that the electrical conductivity of an oxide semiconductor, which is strongly dependent on oxygen non-stoichiometry, can be modulated by utilizing the redox reaction between H$^+$/OH$^-$ ions and the oxide surface. However, water electrolysis and the redox reaction do not take place, because no electric field can be applied on the insulating oxide surface in the first place. Thus, the surface of the oxide must be conductive, as schematically shown in Figure 1b.

We have found that water-infiltrated nanoporous glass overcomes this problem and switches an oxide semiconductor from an insulator to a metal. Electron accumulation, water electrolysis and redox take place successively on an oxide surface at room temperature (RT), leading to the formation of a thin metal layer on the oxide. We have fabricated a field-effect transistor (FET) structure with source, drain and gate electrodes on an insulating oxide, using water-infiltrated nanoporous glass as the gate insulator. First, the insulating oxide surface becomes slightly conductive by applying the gate voltage because of electrostatic charge accumulation. Then, water electrolysis occurs between the gate and the oxide surface. Finally, a redox reaction takes place between H$^+$/OH$^-$ ions and the oxide surface. As a result, a thin metal layer is formed on an insulating oxide.

The key material to make the best use of the electron activity of water is nanoporous glass. We chose amorphous 12CaO·7Al$_2$O$_3$ (a-C12A7) with a nanoporous structure for this purpose. C12A7 is an abundant and environmentally benign material. Crystalline C12A7 becomes semiconducting[9] or metallic[10,11] when the clathrated free oxygen ions (O^{2-}), which are incorporated into the cage structure ($\sim$0.4 nm in diameter), are removed by chemical reduction treatment. On the other hand, 'amorphous' C12A7 is a good electrical insulator, because amorphous C12A7 does not have a cage structure, we therefore ruled out the possibility of electrical conductivity of an

amorphous C12A7 film. As C12A7 can be hydrated easily[12], it is used commercially as a major constituent of aluminous cement. In 1987, Hosono and Abe[13] found that a large amount of bubbles was generated in an a-C12A7 glass, when C12A7 melt was quenched under high oxygen pressure. In the present study, we develop a method to fabricate a-C12A7 film with nanoporous structure (CAN, hereafter) by pulsed laser deposition.

In this study, we show that water-infiltrated CAN electrically switches an oxide semiconductor from insulator to metal, using a CAN-gated FET structure on a SrTiO$_3$ single crystal (Fig. 2a) as a proof of concept. Although SrTiO$_3$ is a wide bandgap ($\sim$3.2 eV) insulator, it becomes n-type conducting SrTiO$_{3-\delta}$ by appropriate reducing treatments[5]. Conducting SrTiO$_3$, especially when it is a two-dimensional (2D) conductor[14,15], is of great importance as an active material for future electronic devices[16], because it has several potential advantages over conventional semiconductor-based electronic materials, such as transparency[17], giant magnetoresistance[18] and giant thermopower[19]. On applying positive gate voltage to the CAN-gated SrTiO$_3$ FET, electron accumulation, water electrolysis and electrochemical reduction occur successively on the SrTiO$_3$ surface at RT. This leads to the formation of a thin ($\sim$3 nm) metal layer with an extremely high electron concentration (10^{15}–10^{16} cm^{-2}), which exhibits exotic thermoelectric behaviour.

Results

Water-infiltrated nanoporous glass (CAN). The trilayer structure composed of Ti (20 nm)/CAN (200 nm)/SrTiO$_3$ is clearly observed in the cross-sectional transmission electron microscopic (TEM) image of the CAN-gated SrTiO$_3$ FET (Fig. 2b). Many brighter contrasts (diameter $\sim$10 nm) are seen throughout the CAN region. Furthermore, several dark contrasts with a diameter $<$10 nm are observed in the Z-contrast, high-angle, annular dark-field scanning TEM (STEM) image of the CAN film (Fig. 2c). Judging from these TEM/STEM images, high-density nanopores with a diameter of $<$10 nm are incorporated into the CAN film.

We subsequently measured thermal desorption spectrum (TDS) of the CAN films to detect weakly bonded chemical species in the nanopores. Most of the desorbed species were H$_2$O (m/z = 18, where m/z indicates the molecular mass to charge ratio; Fig. 2d). The amount of H$_2$O up to 400 °C was estimated to be 1.4$\times$10^{22} cm^{-3}, which corresponds to 41%. The bulk density of the CAN film was $\sim$2.1 g cm^3, evaluated by grazing incidence X-ray reflectivity (Supplementary Fig. S2), which corresponds to 72% of fully dense a-C12A7 (2.92 g cm^3)[20]. From these results, we judged that moisture
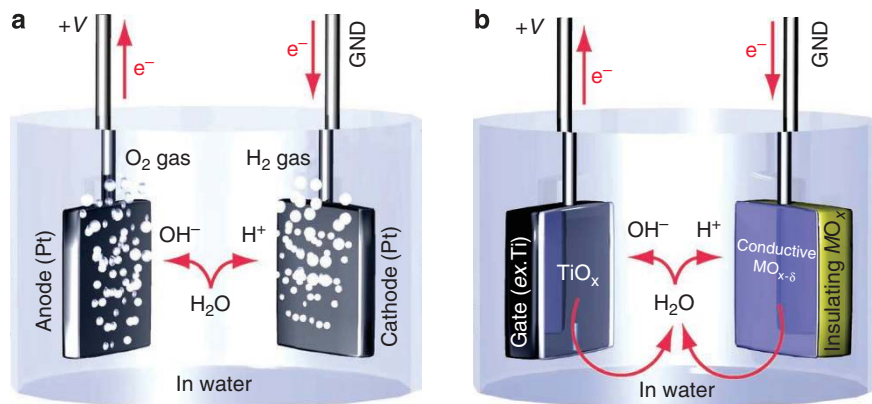

Figure 1 | Field-induced water electrolysis switches an oxide semiconductor from an insulator to a metal. (**a**) Simple water electrolysis with two Pt electrodes as the cathode and anode immersed in water. H$^+$ and OH$^-$ ions, which are generated by the electrolysis, become H$_2$ and O$_2$ gases on the anode and cathode, respectively. (**b**) Water electrolysis with an insulating oxide MO_x, with a slightly conductive surface $MO_{x-\delta}$. Similar to **a**, H$^+$/OH$^-$ ions are attracted to the $MO_{x-\delta}$, leading to the redox reaction between H$^+$/OH$^-$ ions and the $MO_{x-\delta}$ surface. GND, ground.

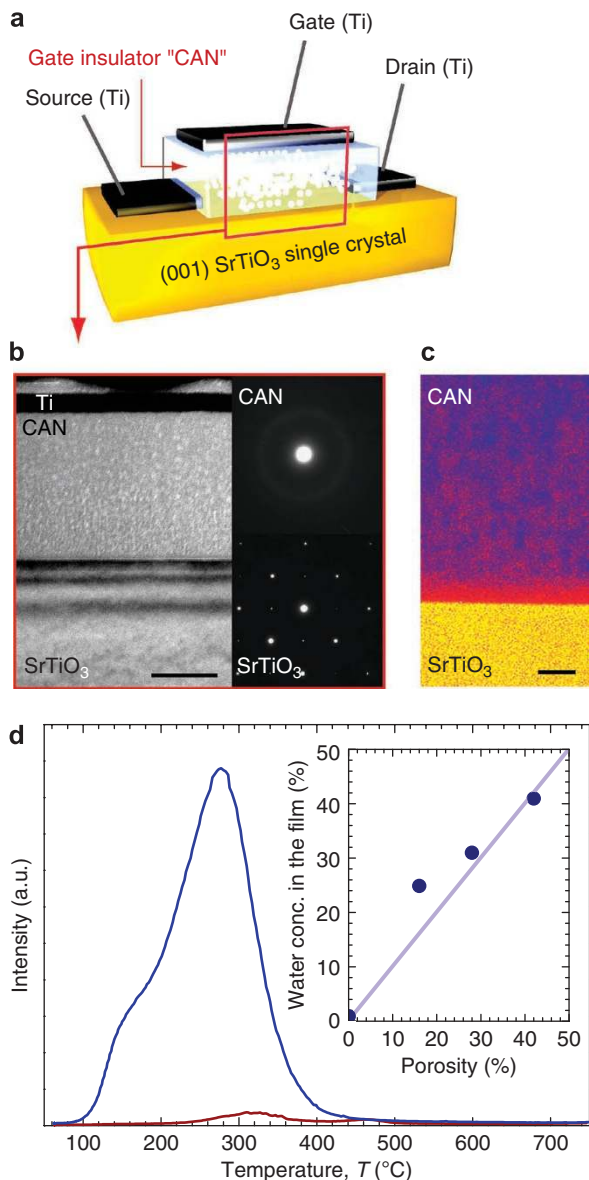**Figure 2 | The CAN-gated SrTiO₃ FET.** (**a**) A schematic illustration of the CAN-gated $SrTiO_3$ FET. (**b**) Cross-sectional TEM image of the CAN-gated $SrTiO_3$ FET (left panel). Scale bar is 100 nm. Trilayer structure composed of Ti/CAN/$SrTiO_3$ is observed. Large amount of light spots are seen in the whole CAN region. Broad halo is observed in the selected area electron diffraction pattern of CAN, and diffraction pattern from $SrTiO_3$ single crystal is also shown below (right panel). (**c**) Z-contrast, high-angle, annular dark-field STEM image of the CAN/$SrTiO_3$ interface. Scale bar is 20 nm. Nanopores with diameter <10 nm appear dark. (**d**) TDS spectrum of water ($m/z = 18$ H_2O) in the CAN film (blue). The amount of H_2O up to 400 °C was estimated to be 1.4×10^{22} cm^{-3} (= 0.41 g cm^{-3}, ~41%). TDS spectrum in the dense a-C12A7 film is shown for comparison (red, 0.009 g cm^{-3}). The water concentration increases monotonically with an increase in the porosity of the CAN films (the inset).

in the air (humidity 40–50%) would infiltrate the CAN film most likely due to the capillary effect, hence, nanopores in the CAN film were filled with water.

Field-induced water electrolysis. We then measured the electron transport properties of the CAN-gated $SrTiO_3$ FET at RT. Figure 3 summarizes (a) drain current (I_d) versus gate voltage (V_g) curves,
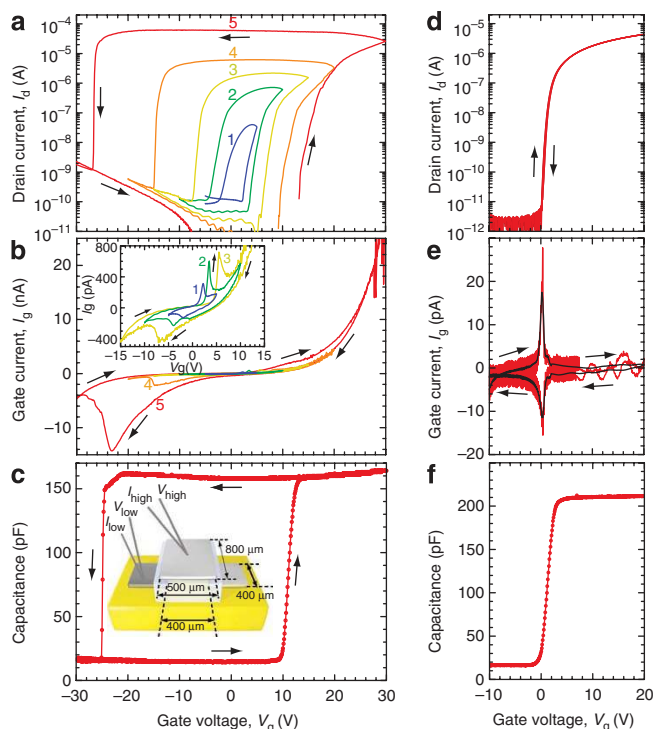

Figure 3 | Electron transport properties of the CAN-gated SrTiO₃ FET at RT. (**a**) I_d versus V_g, (**b**) I_g versus V_g and (**c**) C versus V_g, I_d versus V_g (**d**), I_g versus V_g (**e**), and C versus V_g curves (**f**) of the dense a-C12A7-gated $SrTiO_3$ FET are also shown for comparison. Both the channel length, L, and the channel width, W, are 400 μm. The gate voltage sweeps were performed in numerical order (for example: 1: $-5\,V \to 0\,V \to +5\,V \to 0\,V \to -5\,V$). (**a**) I_d versus V_g curves ($V_d = +2\,V$) show large anticlockwise hysteresis, although very small clockwise hysteresis is seen in the dense one (**d**, $V_d = +1\,V$). (**b**) I_g increases exponentially up to 20 nA with V_g, which is ~10^4 greater than that of the dense a-C12A7-gated $SrTiO_3$ FET (**e**, red: observed, grey: smoothed). (**c**) The C versus V_g curve shows a large anticlockwise hysteresis loop. The maximum C (frequency: 20 Hz) of the nanoporous a-C12A7-gated $SrTiO_3$ FET is ~160 pF, ~76% of that of the dense a-C12A7-gated $SrTiO_3$ FET ((**f**) ~210 pF).

(b) gate current (I_g) versus V_g curves, and (c) capacitance (C) versus V_g curve of the CAN-gated $SrTiO_3$ FET. Corresponding properties of the dense a-C12A7-gated $SrTiO_3$ FET[21] (d, e, f) were also measured for comparison. Both the channel length, L, and the channel width, W, were 400 μm. Dielectric permittivity (ε_r) of a-C12A7 was 12[21]. The gate voltage sweeps were performed in numerical order (for example: 1: $-5\,V \to 0\,V \to +5\,V \to 0\,V \to -5\,V$). The I_d versus V_g curves (a) show large anticlockwise hysteresis, indicating movement of mobile ions[22], though very small clockwise hysteresis (~0.5 V) is seen in the dense a-C12A7-gated $SrTiO_3$ FET (d). Although very small, I_g (~2 pA) is observed in the dense a-C12A7-gated $SrTiO_3$ FET (e), whereas the I_g of the CAN-gated $SrTiO_3$ FET (b) increases exponentially up to 20 nA with V_g, suggesting that mobile ions transport electronic charge. The C versus V_g curve (c) of the CAN-gated $SrTiO_3$ FET shows large anticlockwise hysteresis loop. The maximum C is ~160 pF, ~76% of the value for the dense a-C12A7-gated $SrTiO_3$ FET ((f) ~210 pF), consistent with the fact that the volume fraction of dense a-C12A7 part in the CAN film is ~72%.

We also observed a clear pinch-off and saturation in I_d at low V_g region (see Supplementary Fig. S3), indicating that the operation of this FET conformed to standard FET theory at low gate voltage. Thus, we concluded that first the insulating $SrTiO_3$ surface became slightly conductive with gate voltage because of the
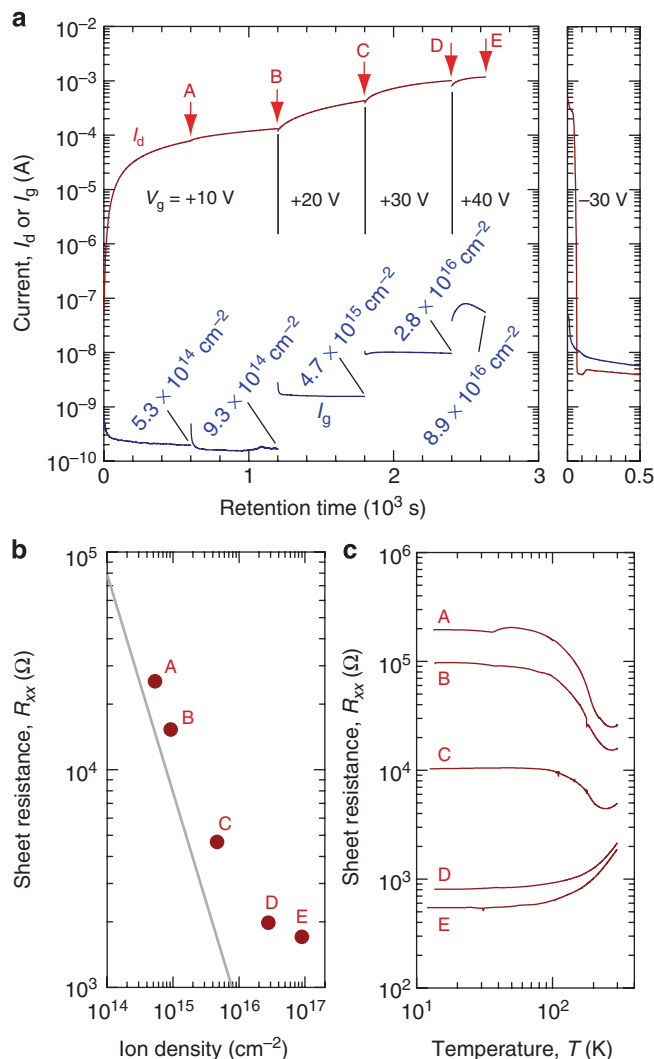
a

b

c

Figure 4 | A redox reaction switches an insulating $SrTiO_3$ to metal.
(**a**) Retention time dependences of I_d and I_g for the CAN-gated $SrTiO_3$ FET at several V_g at RT ($V_d = +2$ V). The I_d increases gradually with retention time at constant V_g. Ion density, which is the retention time integral of I_g, reaches ~9×10^{16} cm^{-2} when $V_g = +40$ V is applied. (**b**) R_{xx} versus ion density for the state A–E marked in **a** at RT. The grey line (slope = –1) indicates $R_{xx} = (e \cdot n_{xx} \cdot \mu)^{-1}$, where n_{xx} and μ are ion density, and μ_{FE} (0.8 cm^{2}V^{-1}s^{-1}), which was obtained as in Supplementary Figure S4b. (**c**) Temperature dependence of R_{xx} for the state A–E marked in Figure 4a.

electron charge that was accumulated at the $SrTiO_3$ surface by pure electrostatic effect.

To clarify the role of water in the electrical transport properties, we measured the I_d versus V_g characteristics of the CAN-gated $SrTiO_3$ FET at 0 °C using a Peltier cooler, because H$^+$ and OH$^-$ ions cannot move through ice (Supplementary Fig. S4). The device does not show such large anticlockwise hysteresis at 0 °C. Although the maximum C increased from ~160 pF (25 °C) to ~240 pF (0 °C), I_d at $V_g = +10$ V decreased from ~5 μA (25 °C) to ~1 μA (0 °C), most likely because of the fact that water in the CAN acts as a simple gate dielectric at 0 °C ($\varepsilon_{r\,25°C}$ ~78, $\varepsilon_{r\,0°C}$ ~88)[23]. The field-effect mobility (μ_{FE}) value of the FET at 0 °C is ~0.8 cm^{2}V^{-1}s^{-1}, which is comparable to that of the dense a-C12A7-gated $SrTiO_3$ FET (~2 cm^{2}V^{-1}s^{-1}), obtained from $\mu_{FE} = g_m((C \times V_d)/(W \times L))^{-1}$, where g_m was the transconductance $\partial I_d/\partial V_g$. We also measured Hall mobility (μ_{Hall}) of a CAN-gated $SrTiO_3$ FET after several V_g applications (metallic state) and obtained μ_{Hall} values of 2.3–2.5 cm^{2}V^{-1}s^{-1}, which is approximately
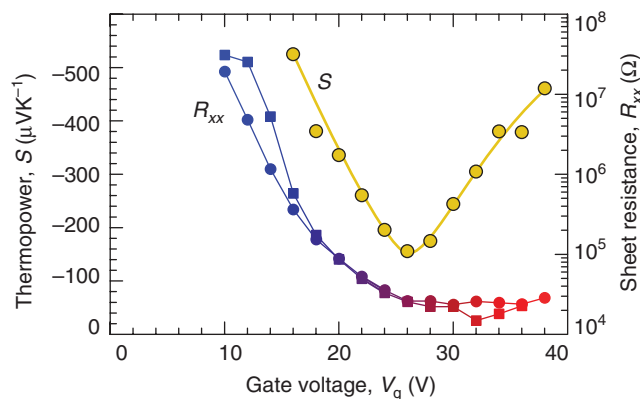
Figure 5 | Thermopower and sheet resistance as a function of applied V_g.

Novel thermopower behaviour: V-shaped turnaround of S is seen, though R_{xx} (circle: before S measurement, square: after S measurement) decreases gradually as V_g increases, probably due to transition of electronic nature from 3D to 2D in the interface region.

three times larger than the μ_{FE} value (~0.8 cm^{2}V^{-1}s^{-1}). These results clearly indicate that H$^+$ and OH$^-$ ions in the CAN are the main contributors to electron transport at RT.

Insulator-to-metal switching. We then observed the electrochemical redox reaction of $SrTiO_3$. Figure 4a shows the changes of I_d and I_g during V_g sweep from +10 to +40 V, as a function of retention time. The I_d gradually increases with retention time. The rate of I_d increase grows with V_g. The I_g also increases with V_g. The I_d reaches ~1 mA at $V_g = +40$ V. The I_d decreases drastically when negative V_g of −30 V is applied.

The sheet resistance (R_{xx}) at several points (A–E) was plotted as a function of ion density, which was obtained by $I_g \times t$ (Fig. 4b). The observed values were close to the grey line, which is $R_{xx} = (e \cdot n_{xx} \cdot \mu)^{-1}$, where n_{xx} and μ are ion density, and μ_{FE} (0.8 cm^{2}V^{-1}s^{-1}) was obtained as in Supplementary Figure S4b, suggesting that carrier electrons were generated as a result of the electrochemical reduction of $SrTiO_3$. Although samples A–C exhibit insulating $R_{xx} - T$ behaviour, D and E exhibit metallic $R_{xx} - T$ behaviour (Fig. 4c).

Exotic thermopower. We have also shown that the metal layer on the $SrTiO_3$ in the FET exhibits novel thermoelectric behaviour: V-shaped turnaround of S is seen, although R_{xx} decreases gradually as V_g increases (Fig. 5). As we have reported previously, $|S|$ value enhancement of electron-doped $SrTiO_3$ can be observed when the conducting layer thickness is <~3 nm[19], probably because of 2D effect[24], where the thermal de Broglie's wavelength of conduction electrons in $SrTiO_3$ is ~6 nm[25]. We therefore expected that 2D $|S|$ can be observed at high V_g, because the layer thickness may become thinner.

When the V_g was <+26 V, $|S|$ value gradually decreased with V_g. Similar $|S|$ behaviour, which can be analysed using simple three-dimensional (3D) electron diffusion theory, was also observed in the dense a-C12A7-gated $SrTiO_3$ FET, as shown in Supplementary Figure S5. Thus, we used the 3D electron diffusion theory[26] to analyse the layer thickness. The 3D electron concentrations (n_{3D}) at $V_g = +16$, +20 and +26 V were estimated to be ~1.5×10^{19}, 1.5×10^{20} and ~1.1×10^{21} cm^{-3}, respectively. The n_{xx} values at $V_g = +16$, +20 and +26 V, which can be calculated using R_{xx} and μ_{FE} (0.8 cm^{2}V^{-1}s^{-1}), are 1.4×10^{13}, 9.0×10^{13} and 3.3×10^{14} cm^{-2}, respectively, suggesting that the $SrTiO_{3-\delta}$ thicknesses (~n_{xx}/n_{3D}) are ~9, 6 and 3 nm, respectively, confirming that the observed S obeys simple 3D electron diffusion theory. On the contrary, when the $V_g > 26$ V was applied, the $|S|$ value increased. The conducting layer thickness

may be < 3 nm, the observed upturn at $V_g > 26$ V is most likely due to 2D effect[19,24].

Discussion

The present CAN-gated SrTiO₃ FET has several merits compared with established methods such as thermal reduction[5], ion irradiation[17,27], thin film growth[14,15,17,18] and simple FET[21,28], which are often utilized to switch an insulating SrTiO₃ to a metal. This is because the current method allows a metal layer to be easily fabricated with extremely low energy. First, required electricity is extremely less (~50 μW cm⁻² for 'D' in Fig. 4) compared with that of thermal reduction (~kW) and ion implantation (~W cm⁻²). Second, an extremely thin (~3 nm) metal layer, which exhibits exotic thermopower (Fig. 5), can be fabricated. Normally, such thin layers must be fabricated through complicated vapour phase epitaxy methods, such as pulsed laser deposition and molecular beam epitaxy. Third, our CAN-gated SrTiO₃ FET exhibits a nonvolatile metal or highly conductive/insulator transition (Figs 3a and 4a and Supplementary Fig. S6), because a reversible redox reaction is utilized in addition to the field effect.

Although several efficient gating methods using liquid electrolytes have been proposed very recently[28–31], we would like to argue that the present water-infiltrated nanoporous glass 'CAN' is truly superior to the liquid-based gate dielectrics. Liquid electrolytes including 'gel' would be very useful to electrostatically accumulate carriers at the transistor channel by applying rather low V_g (a few volts) using their huge capacitance. However, they would not be suitable for practical applications without sealing because of liquid leakage problem. Our 'CAN' is a chemically stable rigid glassy solid with a higher decomposition voltage, showing excellent adhesion with chemically robust oxide such as SrTiO₃ surface and no liquid (water) leakage occurs. Carrier injection/discharge can be controlled by V_g as redox reaction, which occurs at the interface of H⁺ or OH⁻/semiconductor, is utilized for carrier injection/discharge, though rather high V_g (several ten volts) should be required for Redox reaction. Further, we observed novel thermopower behaviour: V-shaped turnaround, probably due to transition of electronic nature from 3D to 2D in the interface region, as the FET could be operated at high V_g. These clearly indicate the effectiveness of our 'CAN'.

In summary, we have demonstrated that water, when it infiltrates nanoporous glass, can switch an insulating oxide to metal. As an example, we have built a FET on an insulating oxide, SrTiO₃, using water-infiltrated nanoporous glass, amorphous 12CaO·7Al₂O₃ with nanoporous structure 'CAN' as the gate insulator. First, the insulating SrTiO₃ surface became slightly conductive with gate voltage because of electrostatic charge accumulation. Then, H⁺/OH⁻ ions were generated due to water electrolysis occurring between the gate and the SrTiO₃ surface. Subsequently, a redox reaction took place between H⁺/OH⁻ ions and the SrTiO₃ surface. As a result, a thin metal (~3 nm) layer with extremely high electron concentration of 10^{15}–10^{16} cm⁻² was formed on the insulating SrTiO₃. The electron activity of water, as it infiltrates nanoporous glass 'CAN', may find many useful applications in electronics or energy storage.

Methods

Fabrication of the CAN-gated SrTiO₃ FET. The FET structures (Fig. 2a) were fabricated on the (001)-face of SrTiO₃ single crystal plate (10×10×0.5 mm, SHINKOSHA), treated in NH₄F-buffered HF (BHF) solution[32]. First, 20-nm-thick metallic Ti films, used as the source and drain electrodes, were deposited through a stencil mask by electron beam evaporation (base pressure ~10⁴ Pa, no substrate heating/cooling) onto the SrTiO₃ plate. Ohmic contact between the Ti and SrTiO₃ surface was confirmed by conventional I–V characteristics (output characteristics), as shown in Supplementary Figure S3b. Then, a 200-nm-thick CAN film was deposited through a stencil mask by pulsed laser deposition (KrF excimer laser, fluence ~3 J cm² per pulse) at RT using dense polycrystalline C12A7 ceramic as target. During the CAN deposition, the oxygen pressure in the deposition chamber was kept at 5 Pa. Finally, a 20-nm-thick metallic Ti film, used as the gate electrode, was deposited through a stencil mask by electron beam evaporation.

Analysis of the CAN films. The bulk density and thickness of the CAN films were evaluated by grazing incidence X-ray reflectivity (ATX-G, Rigaku). Microstructures of the CAN films were observed by using TEM (JEOL JEM-2010, acceleration voltage = 200 kV) and aberration-corrected STEM (JEOL JEM-2100F, acceleration voltage = 200 kV). Water concentration in the CAN films was analysed by TDS measurements (TDS1200, ESCO). The TDS measurements were carried out in a vacuum chamber with the background pressure of ~10⁻⁷ Pa at varied temperatures from 60 to 700 °C at a heating rate of 60 °C per min.

Electron transport properties. Electrical properties of the FETs were measured by using a semiconductor device analyser (B1500A, Agilent). The capacitance of the CAN layer on the FETs was measured using an LCR meter (4284A, Agilent). The thermopower (S) values were measured using two Peltier devices under the FET to give a temperature difference between the source and drain electrodes (Supplementary Fig. S7). Two thermocouples (K-type) located at both ends of the channel were used for monitoring the temperature difference (ΔT, 0–5 K). S values were measured after each V_g sweep (for example: V_g application 0 V→ + 16 V→0 V→S measurements).

References

1. Trasatti, S. 1799–1999: Alessandro Volta's 'Electric pile' two hundred years, but it doesn't seem like it. *J. Electroanal. Chem.* **460,** 1–4 (1999).
2. Light, T. S., Licht, S., Bevilacqua, A. C. & Morash, K. R. The fundamental conductivity and resistivity of water. *Electrochem. Solid-State Lett.* **8,** E16–E19 (2005).
3. Zunger, A. *n*-type doping of oxides by hydrogen. *Appl. Phys. Lett.* **81,** 73–75 (2002).
4. Van de Walle, C. G. Hydrogen as a cause of doping in zinc oxide. *Phys. Rev. Lett.* **85,** 1012–1015 (2000).
5. Frederikse, H. P. R., Thurber, W. R. & Hosler, W. R. Electronic transport in strontium titanate. *Phys. Rev.* **134,** A442–A445 (1964).
6. Breckenridge, R. G. & Hosler, W. R. Electrical properties of titanium dioxide semiconductors. *Phys. Rev.* **91,** 793–801 (1953).
7. Hosono, H., Kikuchi, N., Ueda, N., Kawazoe, H. & Shimidzu, K. Amorphous transparent electroconductor 2CdO·GeO₂: conversion of amorphous insulating cadmium germanate by ion implantation. *Appl. Phys. Lett.* **67,** 2663–2665 (1995).
8. Miyakawa, M., Hayashi, K., Hirano, M., Toda, Y., Kamiya, T. & Hosono, H. Fabrication of highly conductive 12CaO·7Al₂O₃ thin films encaging hydride ions by proton implantation. *Adv. Mater.* **15,** 1100–1103 (2003).
9. Hayashi, K., Matsuishi, S., Kamiya, T., Hirano, M. & Hosono, H. Light-induced conversion of an insulating refractory oxide into a persistent electronic conductor. *Nature* **419,** 462–465 (2002).
10. Matsuishi, S. *et al.* High-density electron anions in a nanoporous single crystal: [Ca₂₄Al₂₈O₆₄]⁴⁺(4e⁻). *Science* **301,** 626–629 (2003).
11. Kim, S.- W. *et al.* Metallic state in a lime-alumina compound with nanoporous structure. *Nano Lett.* **7,** 1138–1143 (2007).
12. Hayashi, K., Hirano, M. & Hosono, H. Thermodynamics and kinetics of hydroxide ion formation in 12CaO·7Al₂O₃. *J. Phys. Chem.* **B109,** 11900–11906 (2005).
13. Hosono, H. & Abe, Y. An oxygen-effervescent aluminate glass. *J. Am. Ceram. Soc.* **70,** C38–C39 (1987).
14. Ohtomo, A. & Hwang, H. Y. A high-mobility electron gas at the LaAlO₃/SrTiO₃ heterointerface. *Nature* **427,** 423–426 (2004).
15. Kozuka, Y., Kim, M., Bell, C., Kim, B. G., Hikita, Y. & Hwang, H. Y. Two-dimensional normal-state quantum oscillations in a superconducting heterostructure. *Nature* **462,** 487–490 (2009).
16. Mannhart, J. & Schlom, D. G. Oxide interfaces–an opportunity for electronics. *Science* **327,** 1607–1611 (2010).
17. Reagor, D. W. & Butko, V. Y. Highly conductive nanolayers on strontium titanate produced by preferential ion-beam etching. *Nat. Mater.* **4,** 593–596 (2005).
18. Brinkman, A. *et al.* Magnetic effects at the interface between non-magnetic oxides. *Nat. Mater.* **6,** 493–495 (2007).
19. Ohta, H. *et al.* Giant thermoelectric Seebeck coefficient of a two-dimensional electron gas in SrTiO₃. *Nat. Mater.* **6,** 129–134 (2007).
20. Kim, S.- W., Toda, Y., Hayashi, K., Hirano, M. & Hosono, H. Synthesis of a room temperature stable 12CaO·7Al₂O₃ electride from the melt and its application as an electron field emitter. *Chem. Mater.* **18,** 1938–1944 (2006).
21. Ohta, H. *et al.* Field-modulated thermopower in SrTiO₃-based field-effect transistors with amorphous 12CaO·7Al₂O₃ glass gate insulator. *Appl. Phys. Lett.* **95,** 113505 (2009).
22. Sze, S. M. *Semiconductor Devices: Physics and Technology* 2nd edn. (John Wiley & Sons, 2002).
23. Buchner, R., Barthel, J. & Stauber, J. The dielectric relaxation of water between 0°C and 35°C. *Chem. Phys. Lett.* **306,** 57–63 (1999).
24. Hicks, L. D. & Dresselhaus, M. S. The effect of quantum well structures on the thermoelectric figure of merit. *Phys. Rev. B* **47,** 12727–12731 (1993).
25. Mune, Y., Ohta, H., Koumoto, K., Mizoguchi, T. & Ikuhara, Y. Enhanced Seebeck coefficient of quantum-confined electrons in SrTiO₃/SrTi₀.₈Nb₀.₂O₃ superlattices. *Appl. Phys. Lett.* **91,** 192105 (2007).

26. Vining, C. B. A model for the high-temperature transport properties of heavily doped n-type silicon-germanium alloys. *J. Appl. Phys.* **69,** 331–341 (1991).
27. Kan, D. *et al.* Blue-light emission at room temperature from Ar$^+$ irradiated SrTiO$_3$. *Nat. Mater.* **4,** 816–819 (2005).
28. Ueno, K. *et al.* Electric-field-induced superconductivity in an insulator. *Nat. Mater.* **7,** 855–858 (2008).
29. Yuan, H., Shimotani, H., Tsukazaki, A., Ohtomo, A., Kawasaki, M. & Iwasa, Y. High-density carrier accumulation in ZnO field-effect transistors gated by electric double layers of ionic liquids. *Adv. Funct. Mater.* **19,** 1046–1053 (2009).
30. Kergoat, L. *et al.* A water-gate organic field-effect transistor. *Adv. Mater.* **22,** 2565–2569 (2010).
31. Heller, I. *et al.* Charge noise in grapheme transistors. *Nano Lett.* **10,** 1563–1567 (2010).
32. Kawasaki, M. *et al.* Atomic control of the SrTiO$_3$ crystal surface. *Science* **266,** 1540–1542 (1994).

Acknowledgments

Author contributions

Additional information